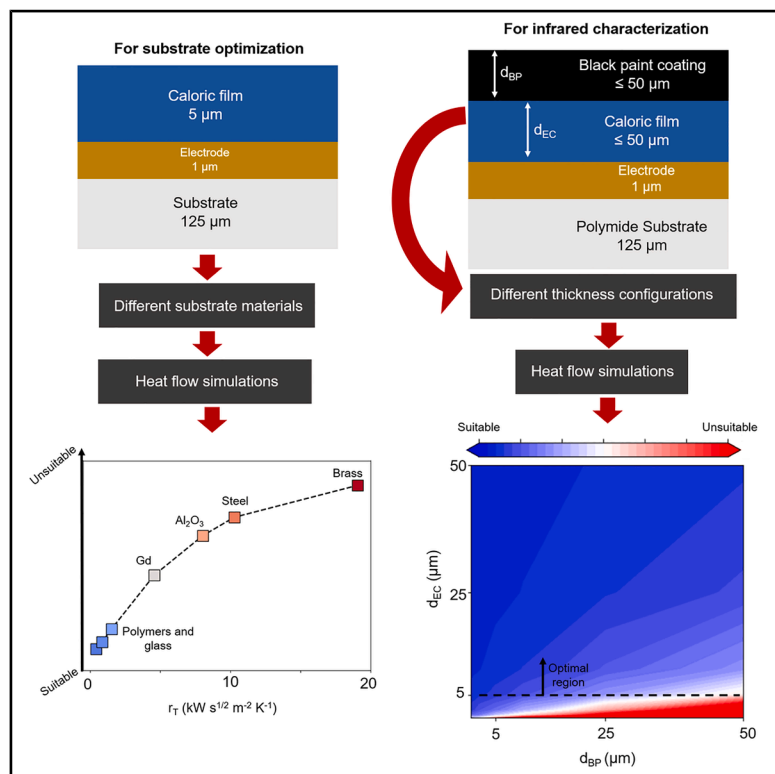


Roadmap for electrocaloric films characterization

Graphical abstract



Authors

Victor Regis, Urban Tomc,
Andrej Kitanovski, Hana Uršič

Correspondence

hana.ursic@ijs.si

In brief

Simulation in materials science, Materials characterization techniques, Films

Highlights

- Thick-film structures were simulated targeting maximized caloric response
- Substrates with low thermal effusivity ($\leq 3 \text{ kW s}^{1/2} \text{ m}^{-2} \text{ K}^{-1}$) are suitable
- Substrates with low thermal conductivity ($\leq 1 \text{ W K}^{-1} \text{ m}^{-1}$) are suitable
- Numerical simulations for infrared-based caloric measurements were performed



Article

Roadmap for electrocaloric films characterization

Victor Regis,^{1,2} Urban Tomc,³ Andrej Kitanovski,³ and Hana Uršič^{1,2,4,*}¹Electronic Ceramics Department, Jožef Stefan Institute, Jamova cesta 39, 1000 Ljubljana, Slovenia²Jožef Stefan International Postgraduate School, Jamova cesta 39, 1000 Ljubljana, Slovenia³Faculty of Mechanical Engineering, University of Ljubljana, Askerceva cesta 6, 1000 Ljubljana, Slovenia⁴Lead contact*Correspondence: hana.ursic@ijs.si<https://doi.org/10.1016/j.isci.2026.115965>

SUMMARY

The development of electrocaloric (EC) elements for cooling technologies has progressed by integrating the EC layers onto various substrates. However, a precise understanding of heat losses on direct characterization methods is still lacking, particularly in the infrared (IR) camera method. In this work, we perform numerical simulations on EC film structures to benchmark the substrate influence on the cooling output of the structure for characterization purposes. Substrates with low thermal effusivity ($\leq 3 \text{ kW s}^{1/2} \text{ m}^{-2} \text{ K}^{-1}$) exhibit minimal influence on the output of films. Simulations were also performed to investigate the impact of EC film and black-paint coating thicknesses on the correction factor for IR characterization methods. A single-digit correction factor can be achieved if the EC film is thicker than the coating. Our results offer a roadmap for designing EC structures for cooling at the micro-to-nano scales.

INTRODUCTION

Vapor compression cooling technologies, although widespread and well-established, have a limited Carnot efficiency and do not offer a viable way to be miniaturized at micro or nano scales. In the last few decades, research on cooling alternatives has intensified, particularly on the materials that exhibit caloric effects, which are the adiabatic and reversible temperature change (ΔT_{AD}) as a response to external stimuli. Such materials are categorized into electrocalorics (ECs), magnetocalorics, or mechanocalorics, which are responsive to electric field, magnetic field, or mechanical load, respectively.^{1–4} Particularly, ECs show a promising future for miniaturized cooling devices, as these only require the material layers, electrodes, and the voltage supply, all of which are already present in electronic devices.⁴ The most prominent ECs are Pb-based oxides, such as $\text{Pb}(\text{Mg}_{1/3}\text{Nb}_{2/3})\text{O}_3\text{-xPbTiO}_3$ and $\text{Pb}(\text{Sc}_{0.5}\text{Ta}_{0.5})\text{O}_3$.^{5–13} In particular, $0.9\text{Pb}(\text{Mg}_{1/3}\text{Nb}_{2/3})\text{O}_3\text{-0.1PbTiO}_3$ (PMN-10PT) has been extensively studied for its thermal properties as well as its excellent EC performance in film⁸ and ceramic^{13–16} forms.

EC films are promising for micro-cooling applications as they have been shown to achieve large ΔT_{AD} ,^{4–8} and can be integrated onto a variety of substrates: polymers,^{7–9} metals,^{17–20} glasses,^{19–21} and ceramics.^{21–23} Caloric-based prototypes require excellent thermal properties in order to achieve optimal performance.^{24–28} However, for characterization purposes, low thermal transport properties are required, otherwise the substrate will absorb all the caloric output, hindering the measurement. In other words, for a reliable quantification and understanding of the intrinsic properties of caloric materials, it is necessary to minimize systematic heat losses, therefore maximizing the measurement response.^{8,29} In light of this, in recent years, research

has focused on finding and optimizing substrates that allow for maximized measurement responses. Despite that, most reports which discuss heat sink effects for characterization purposes consider only case-specific parameters and, to the authors' knowledge, there is no study on the impact of substrate thermal parameters, such as heat capacity (c_p), thermal conductivity (λ), and density (ρ), on the effective cooling output of caloric film structures, particularly for characterization purposes.

Characterization methods of the caloric response of materials are generally classified as either direct or indirect. The indirect approach offers a benchmark ΔT_{AD} value, however it does not take into consideration effects such as Joule heating and heat losses to the substrate, resulting in potentially inaccurate values.⁸ To circumvent such an issue, direct characterization methods can be performed. A common drawback of direct methods is the heat losses related to the measurement setup; in other words, the intrinsic ΔT_{AD} is proportional to the measured temperature change (ΔT_M) by a constant k , called the correction factor. Mathematically, it can be described as $\Delta T_{AD} = k \Delta T_M$, where k can be determined by assessing method-specific experimental parameters. For example, the thermistor-in-calorimeter method requires wiring, a bead-thermistor, glue and has an acquisition time of ~ 1 s, which leads to a factor of 30–50.^{8,9} The correction factor can be significantly reduced by means of a non-contact infrared (IR) characterization method, which has been typically used for magnetocaloric and elastocaloric characterizations.^{30–37} Using the IR method, only a thin layer of a high-emissivity coating, generally black paint, is required, and the acquisition time may be as fast as ~ 1 ms.^{29–31} It has been shown that the IR characterization method can also be used in EC thick films. With the method, single-digit k -values have been achieved on μm -thick EC films prepared on polymer substrates.^{7,8,29}



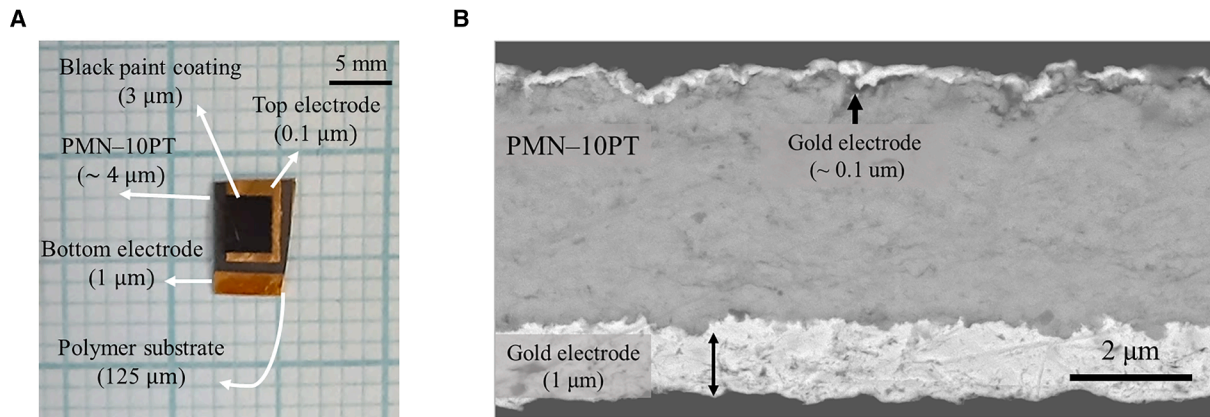


Figure 1. Photograph and microstructure images of the reference sample

(A) Photograph of PMN-10PT thick film on gold-sputtered polymer substrate covered with gold top electrode and coated with black paint layer for IR characterization. The scale bar represents 5 mm.
(B) SEM image of a sample in cross-sectional view. The scale bar represents 2 μm . Note the large thickness difference between the top and bottom electrodes.

In recent years, the IR method has become more widespread, with a wide range of samples being characterized. However, most studies do not report the thickness of the paint, and many do not consider the influence of the black coating on the measurements, likely assuming that the correction factor is negligible.^{38–40} In other studies, targeting the direct characterization of EC μm -thick films, the EC film thickness (d_{EC}) and black paint coating (d_{BP}) are both considered and simulated, albeit only using case-specific parameters.^{8,29} Although the literature reports consistent and accurate results, the influence of d_{EC} and d_{BP} on the correction factor remains unaddressed.

In light of this, in this work, using a finite-element model, we numerically investigate the influence of the substrate thermal parameters on the cooling performance of a caloric film structure, aiming to optimize measurement response. Due to its excellent properties, PMN-10PT was chosen as the reference EC material. For the IR method, the impact of the d_{EC} , as well as black coating thicknesses, d_{BP} , on the correction factor k was investigated. This work aims to establish a preliminary assessment on substrate material as well as benchmark sample-to-coating optimization for the IR characterization method of caloric samples.

RESULTS AND DISCUSSION

Numerical model of electrocaloric structures

A typical EC thick-film sample, prepared via the aerosol deposition method, coated for IR characterizations^{7,8} is shown in Figure 1A. Generally, for EC measurements, it is desired to have electrodes as thin as possible to minimize substrate influence. However, in the case of aerosol-deposited samples, due to processing constraints, the bottom electrode must be at least 1 μm -thick to ensure proper film adhesion.^{8,22} Such a structure was used as a reference geometry for the simulations. A scanning electron microscopy image of a sample in a cross-sectional view is shown in Figure 1B.

The investigations were performed via a 2-dimensional finite-element model using COMSOL multiphysics within the

interval 0 s to 50 ms at 10 μs steps. The simulations were then split into two segments: minimizing the influence of the substrate and minimizing the correction factor for IR camera measurements. For the former, d_{EC} was fixed at 5 μm , and different values of ρ , c_p , and λ were investigated. For the latter, an additional d_{BP} atop of the previous structure was implemented, and polyimide was set as the substrate material. Structures with different combinations of d_{EC} and d_{BP} were simulated, with both values within 0.5 μm and 50 μm . The simulated structures are schematically shown in Figure 2. The EC effect was implemented through the power density, P_{EC} , described as follows^{8,29}:

$$P_{\text{EC}} = \begin{cases} 0, & t < 10 \mu\text{s} \\ \frac{\rho C_p \Delta T_{\text{AD}}}{\tau}, & 10 \mu\text{s} \leq t \leq \tau \\ 0, & t > \tau_{\text{pul}} \end{cases} \quad (\text{Equation 1})$$

where τ is the duration of the caloric pulse, and it was set to 1 ms to simulate a fast thermal exchange rate.

It should be noted that the intrinsic ΔT_{AD} is proportional to the ΔT_{s} , which reaches the surface layer of the system. For the substrate optimization, the proportionality constant, δ , quantifies only the losses to the substrate, henceforth called the heat sink coefficient, defined as:

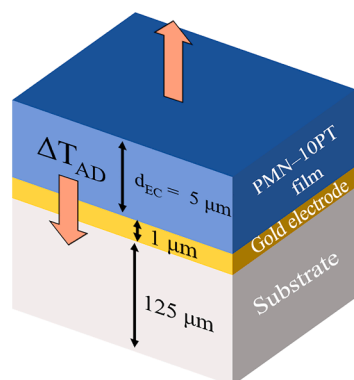
$$\Delta T_{\text{AD}} = \delta \Delta T_{\text{s}} \quad (\text{Equation 2})$$

For IR camera optimizations, the black paint further contributes to the losses. In this case, the intrinsic ΔT_{AD} is proportional to the measured ΔT_{M} by a constant k , which is an experimental parameter conventionally called the correction factor, mathematically described as:

$$\Delta T_{\text{AD}} = k \Delta T_{\text{M}} \quad (\text{Equation 3})$$

For the simulations, PMN-10PT was used as the reference material due to its excellent ΔT_{AD} ^{8,16} as well as moderate thermal properties.¹⁴ To accurately represent the influence of the black

A Substrate optimization



B Black paint optimization

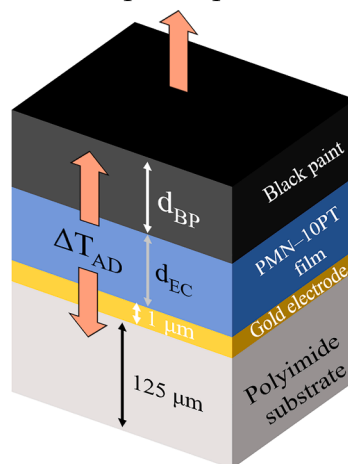


Figure 2. Simulated structures for substrate material and black paint optimizations

Schematic representation of simulated structures for (A) substrate optimization and (B) correction factor optimization. The arrows indicate the heat flow direction after the EC pulse is active.

paint, coatings were prepared using the airbrush method⁴¹ and the black paint c_p was characterized, a value of $1350 \text{ J kg}^{-1} \text{ K}^{-1}$ was measured at room temperature, shown in supplemental information S1. The numerical values of the physical parameters of PMN-10PT, gold, and black paint used in the simulations are shown in Table 1.

Verification of the numerical model

The EC structure model was verified for its numerical consistency by checking the sufficiency of spatial and temporal discretization. For the validation, the structure for IR characterization was selected; in other words, the substrate was set to polyimide, and the black paint layer was considered. In particular, d_{EC} and d_{BP} were set to $5 \mu\text{m}$. As shown in Figure 3A, a number of elements larger than 5×10^4 is needed for the simulations to converge. Figure 3B shows k values as a function of different temporal resolutions, with $100 \mu\text{s}$ being the largest convergent value. Hence, to ensure convergence across all cases, in this work, 7.5×10^4 elements were used and a time resolution of $10 \mu\text{s}$ was implemented. In addition, the calculated Knudsen number of the system was much smaller than 0.01, indicating that the system is in the continuum regime, therefore within converging limits, satisfying the conditions for the heat flow model.^{43–46}

Minimizing the heat sink contribution from the substrate

The heat sink coefficient, δ , quantifies the thermal influence of the substrate material on the cooling performance of the caloric

transfer heat to its surroundings, namely, its thermal effusivity (r_T), mathematically described as^{42,47}:

$$r_T = \sqrt{c_p \lambda \rho} \quad (\text{Equation 4})$$

In the simulations, a wide range of materials was implemented as substrates, namely polymers, metals, silica glass and ceramic Al_2O_3 . As shown Figure 4, substrate materials that exhibit effusivity $r_T \leq 3 \text{ kW s}^{1/2} \text{ m}^{-2} \text{ K}^{-1}$, such as polyimide, polytetrafluoroethylene (PTFE) and silica glass, are the most suitable as such structures can achieve the lowest single-digit δ due to overall poor thermal exchange properties of the substrates. Whereas materials such as Gd, stainless steel, and Al_2O_3 , exhibit $9 < \delta < 15$, in other words, these materials are potentially suitable for the substrates, depending on specific physical parameters of the system and experimental conditions. Among the simulated materials, brass exhibits the largest value of $\delta \sim 18$. The c_p , λ , ρ , r_T of the substrate materials and the corresponding δ of the simulated EC structures are collected in Table 2.

To further assess the substrate influence, the individual contributions of c_p , λ , and ρ of the substrate on the δ values of the systems were also investigated. Using a simulated structure shown in Figure 1A, multiple combinations of the thermal parameter values were investigated. The selected c_p , λ , and ρ values were chosen to represent a wide range of materials for substrates, including polymers, ceramics, and metals.

In the first numerical analysis, c_p of the substrate was set to $450 \text{ J kg}^{-1} \text{ K}^{-1}$ (Figure 5, upper panel). These values approximately correspond to various metals and ceramics. Albeit at low λ , a comparatively low δ can be obtained, metals tend to exhibit larger density compared to ceramics and polymers and large λ , resulting in larger heat sink effects, reaching $\delta \sim 20$. Then, c_p was set to $900 \text{ J kg}^{-1} \text{ K}^{-1}$, representing ceramics and polymers, shown in the middle panel of Figure 5. Particularly, polyimide with $\lambda = 0.2 \text{ W m}^{-1} \text{ K}^{-1}$ and $\rho = 1420 \text{ kg m}^{-3}$ results in $\delta = 2$. In contrast, Al_2O_3 shows a larger thermal conductivity, $\lambda = 30 \text{ W m}^{-1} \text{ K}^{-1}$ and larger density $\rho = 3990 \text{ kg m}^{-3}$, leading to $\delta \sim 15$. Lastly, materials with large c_p ($2500 \text{ J kg}^{-1} \text{ K}^{-1}$) were also simulated, shown in the bottom panel of Figure 5. At large ρ and λ , the coefficient δ can reach values as large as 30.

Table 1. Physical parameters of materials used in the simulations

Parameter	Electrocaloric PMN-10PT ^{8,14}	Gold electrode ^{8,29}	Black paint ^{8,42}
c_p ($\text{J kg}^{-1} \text{ K}^{-1}$)	349	129	1350^{S1}
ρ (kg m^{-3})	8120	19300	1160
λ ($\text{W m}^{-1} \text{ K}^{-1}$)	1.3	318	0.2
ΔT_{AD}	1 K	–	–
τ	1 ms	–	–

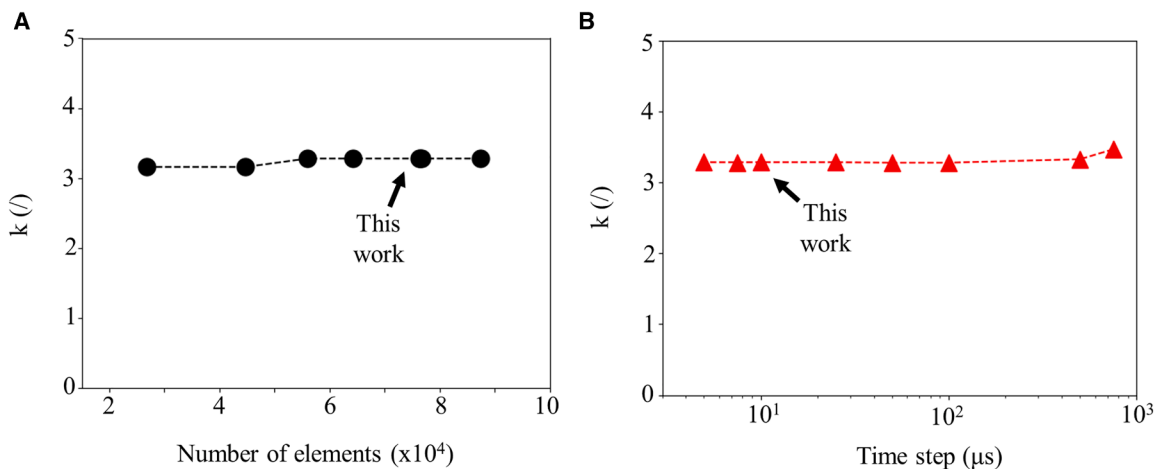


Figure 3. Proof of convergence of simulations

Dependence of the correction factor on (A) the number of elements and (B) the time resolution.

However, at low ρ and λ , for example, in the case of polyethylene that exhibits low density ($\rho < 1420 \text{ kg m}^{-3}$) and low thermal conductivity ($\lambda < 0.5 \text{ W m}^{-1} \text{ K}^{-1}$),^{42,60} the heat sink coefficient results in $\delta < 4$. Notice that in all panels, single-digit δ can be achieved regardless of c_p and ρ , if $\lambda \leq 1 \text{ W m}^{-1} \text{ K}^{-1}$. In other words, a low thermal conductivity of the substrate is a sufficient condition to minimize thermal losses.

Minimizing the correction factor in IR characterizations

The influence of the d_{EC} and the d_{BP} thickness on the correction factor in IR characterizations was investigated. Polyimide ($\rho = 1420 \text{ kg m}^{-3}$, $c_p = 904 \text{ J kg}^{-1} \text{ K}^{-1}$, $\lambda = 0.2 \text{ W m}^{-1} \text{ K}^{-1}$)⁸ was used as a substrate material due to its minimal δ contribution. Simulations were performed with different d_{EC} and d_{BP} combinations, from sub-micron sizes up to $50 \mu\text{m}$, as shown in Figure 2B. The values of k as a function of both d_{EC} and d_{BP} are shown in Figure 6A. Notice that regions of $k \leq 10$ (blue regions)

are more predominant than regions of $k \geq 20$ (red regions), suggesting that increasing d_{EC} plays a more important role in minimizing k than decreasing d_{BP} . Particularly, most of $k \leq 10$ is found above the threshold $d_{\text{EC}} \geq 5 \mu\text{m}$, suggesting that k is strongly dependent on d_{EC} .

Figures 6B and 6C show k as a function of d_{EC} and d_{BP} , respectively. Notice that while k decreases nonlinearly with d_{EC} , it increases linearly with d_{BP} . It should be emphasized that d_{BP} can be as thin as a few μm , while larger thicknesses can be prepared with additional coatings.⁴¹ Assuming $d_{\text{BP}} \leq 40 \mu\text{m}$, in order to achieve single-digit k values, at least one of the following conditions must be satisfied: $d_{\text{EC}} \geq d_{\text{BP}}$ or $d_{\text{EC}} \geq 5 \mu\text{m}$. In bulk materials, $d_{\text{EC}} \gg d_{\text{BP}}$, as the samples are millimeter-thick, while coatings do not exceed the micrometer-range, leading to a negligible correction factor. Thin films, however, generally have $d_{\text{EC}} \leq 0.5 \mu\text{m}$, and the expected correction factor should be considerably large, $k \gg 30$, hindering the IR characterization method as a viable option. In the case of thick-film characterizations, both d_{EC} and d_{BP} are a few micrometers thick, requiring case-specific optimizations in order to obtain $k \leq 10$. In addition, the case of free-standing films is discussed in supplemental information S2. Our results are in good agreement with the literature, where

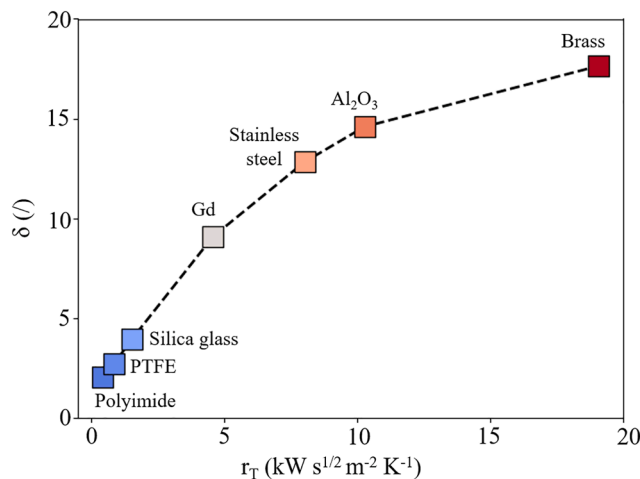


Figure 4. Heat sink coefficient as a function of thermal effusivity

Heat sink coefficient δ as a function of r_T for different materials. Blue markers represent low δ , while red markers represent higher δ values.

Table 2. c_p , λ , and ρ for different substrate materials at 300 K

Material	c_p ($\text{J kg}^{-1} \text{ K}^{-1}$)	λ ($\text{W m}^{-1} \text{ K}^{-1}$)	ρ (kg m^{-3})	r_T ($\text{kW s}^{1/2} \text{ m}^{-2} \text{ K}^{-1}$)	δ (J)
Polyimide ^{8,42}	904	0.1	1420	0.36	2.0
PTFE ⁴⁸⁻⁵⁰	1100	0.3	2200	0.85	2.7
Glass ^{51,52}	750	1.4	2200	1.51	3.9
Gd ^{53,54}	300	8.8	7900	4.57	9.1
Stainless steel ⁴²	500	16.2	7930	8.01	12.8
Al_2O_3 ⁵⁵⁻⁵⁷	880	30	3990	10.26	14.6
Brass ^{42,58,59}	380	111	8600	19.05	17.7

The simulated r_T and δ are also shown.

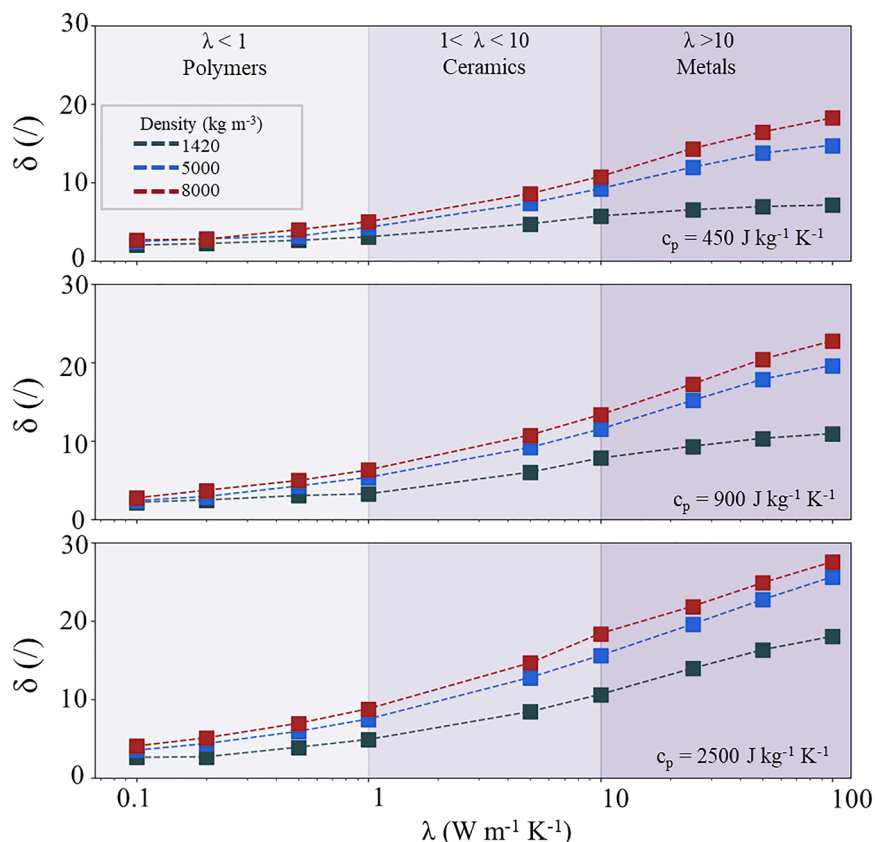


Figure 5. Heat sink coefficient as a function of different thermal parameters

Heat sink coefficient δ as a function of thermal conductivity at different substrate c_p values: $450 \text{ J kg}^{-1} \text{ K}^{-1}$ (upper panel), $900 \text{ J kg}^{-1} \text{ K}^{-1}$ (middle panel), $2500 \text{ J kg}^{-1} \text{ K}^{-1}$ (lower panel). The colored regions within the panels represent the thermal conductivity range of polymers ($\lambda < 1 \text{ W m}^{-1} \text{ K}^{-1}$), ceramics ($1 \text{ W m}^{-1} \text{ K}^{-1} \leq \lambda \leq 10 \text{ W m}^{-1} \text{ K}^{-1}$), and metals ($\lambda > 10 \text{ W m}^{-1} \text{ K}^{-1}$). The marker colors represent different densities. The dashed lines are a guide to the eyes.

a $3\text{-}\mu\text{m}$ -thick PMN-10PT sample with a $3.5\text{-}\mu\text{m}$ -thick coating was estimated to have a $k \sim 3.4$ on a polyimide substrate.⁸ In our simulations, under similar conditions, $k \sim 3.8$ can be obtained. The difference between the values is attributed to the different thermal parameters of the black paints.

It is worth mentioning that in most practical applications, heat loss effects are expected to be larger than those calculated here, as the simulations were performed assuming ideal conditions (thermally insulated, no electrical contacts, low acquisition time), therefore, our values of δ and k represent lower-bound es-

timates. In other words, structures that exhibit large δ values according to our work will likely exhibit large values in real-world applications. In addition, this work is based on PMN-10PT as the active material, and, evidently, distinctive materials will interact differently and should be considered on a case-by-case basis. Further discussion on the influence of different materials, IR camera frame rate, and systematic contributions can be found in supplemental information S3.

In conclusion, using numerical simulation, we have investigated the substrate influence on the EC cooling output of PMN-10PT thick-film structures. Our results indicate that substrate materials with thermal effusivity $r_T \leq 3 \text{ kW s}^{1/2} \text{ m}^{-2} \text{ K}^{-1}$ lead to minimal heat losses. Particularly, the condition $\lambda_{\text{substrate}} \leq 1 \text{ W m}^{-1} \text{ K}^{-1}$, regardless of c_p and ρ , is sufficient to achieve the heat sink coefficient $\delta \leq 10$, while further minimization can be achieved with substrate materials with lower overall r_T . In this manner, we have benchmarked the values for the thermal properties of substrates in the EC thick-film structures targeting optimized caloric performance.

In addition, the influence of the EC layer thickness and d_{BP} thickness on the correction factor for the IR characterization

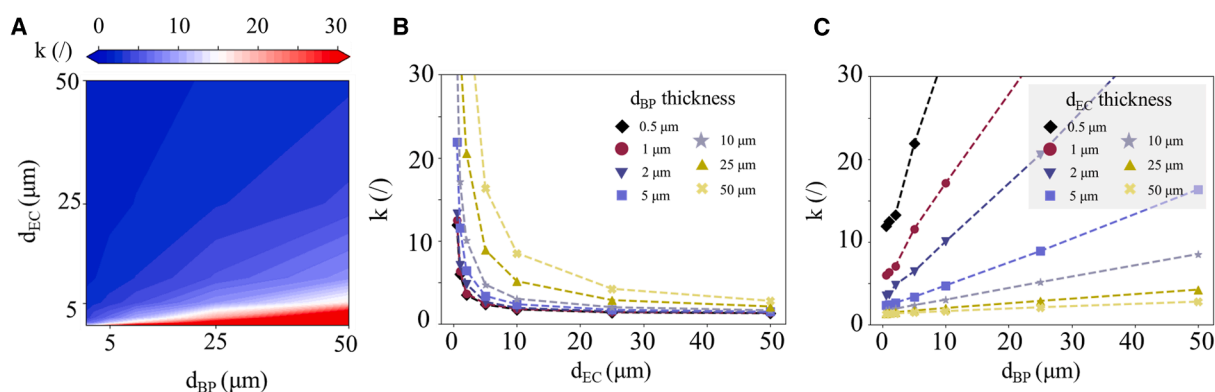


Figure 6. Correction factor as a function of electrocaloric film thickness and black paint thickness

(A) 2D mapping of the correction factor as a function of d_{EC} and d_{BP} . Correction factor k as a function of (B) d_{EC} , and (C) d_{BP} .

method was investigated. Our simulations show that single-digit k can be achieved if at least one of the following conditions is met: if the $d_{EC} \geq 5 \mu\text{m}$, assuming $d_{BP} \leq 40 \mu\text{m}$; or $d_{EC} \geq d_{BP}$, with layers thicker than $1 \mu\text{m}$. Both conditions are satisfied in the case of bulk materials, while fine-tuning is required for the characterization of thick films. Our results confirm that coating methods that can achieve d_{BP} as thin as possible, such as printing and airbrushing, are highly desirable for IR-based characterization techniques.

This work provides a framework for preliminary assessment on substrate materials as well as sample-to-black coating optimization for the IR characterization method, and offers a roadmap for designing and characterizing caloric film structures for cooling at the micro-to-nano scales.

Limitations of the study

The main limitation of the work is the ideal case assumption, which results in lower estimates for the heat sink coefficient and correction factor. While it was briefly discussed in the supplemental information, further adjustments and considerations should be made on a case-by-case basis to ensure an accurate estimate of the parameters. In addition, this work focuses on the reference material PMN-10PT, which shows generally intermediate thermal properties. However, caloric effects can be observed on a diverse range of materials, including polymers (thermal insulators) and metals (thermal conductors). In other words, different thermal behaviors can be expected for different caloric materials and should be taken into consideration accordingly.

RESOURCE AVAILABILITY

Lead contact

Further information and requests for resources should be directed to and will be fulfilled by the lead contact, Prof. Dr. Hana Uršič (hana.ursic@ijs.si).

Materials availability

This study did not generate new unique materials.

Data and code availability

- The data that support the findings of this study are openly available in Zenodo at <https://doi.org/10.5281/zenodo.18233562>, reference number.⁶¹
- This study generated no custom code.
- Any additional information required to analyze the data reported in this study is available from the [lead contact](#) upon request.

ACKNOWLEDGMENTS

The authors acknowledge the financial support of the Slovenian Research and Innovation Agency (projects no. J2-60035, program no. P2-0105, and young researcher project) and the transnational consortium M-ERA.NET for the project Cool BatMan: Battery Thermal Management System Based on High Power Density Digital Microfluidic Magnetocaloric Cooling (no. 9400, Slovenian part of the project is financed by Ministry of Higher Education, Science and Innovation, Slovenia).

AUTHOR CONTRIBUTIONS

Conceptualization: H.U. and V.R.; data curation: V.R.; formal analysis: V.R.; funding acquisition: H.U. and U.T.; investigation: H.U., V.R., U.T., and A.K.; methodology: U.T. and V.R.; resources: H.U.; software: H.U. and V.R.; supervision: H.U.,

U.T., and A.K.; validation: H.U., U.T., and V.R.; writing – original draft: H.U. and V.R.; writing – review and editing: H.U., V.R., U.T., and A.K.

DECLARATION OF INTERESTS

A. Kitanovski is a member of iScience’s Advisory Board and one of the co-guest editors of the special issue “Advanced thermal control: Fundamentals and applications.”

STAR★METHODS

Detailed methods are provided in the online version of this paper and include the following:

- [KEY RESOURCES TABLE](#)
- [METHOD DETAILS](#)
 - Scanning electron microscopy
 - Numerical modelling
- [QUANTIFICATION AND STATISTICAL ANALYSIS](#)

SUPPLEMENTAL INFORMATION

Supplemental information can be found online at <https://doi.org/10.1016/j.isci.2026.115965>.

Received: January 5, 2026

Revised: March 11, 2026

Accepted: April 28, 2026

REFERENCES

1. Shi, J., Han, D., Li, Z., Yang, L., Lu, S.G., Zhong, Z., Chen, J., Zhang, Q.M., and Qian, X. (2019). Electrocaloric Cooling Materials and Devices for Zero-Global-Warming-Potential, High-Efficiency Refrigeration. *Joule* 3, 1200–1225. <https://doi.org/10.1016/j.joule.2019.03.021>.
2. Moya, X., Kar-Narayan, S., and Mathur, N.D. (2014). Caloric materials near ferroic phase transitions. *Nat. Mater.* 13, 439–450. <https://doi.org/10.1038/nmat3951>.
3. Klinar, K., Law, J.Y., Franco, V., Moya, X., and Kitanovski, A. (2024). Perspectives and Energy Applications of Magnetocaloric, Pyromagnetic, Electrocaloric, and Pyroelectric Materials. *Adv. Energy Mater.* 14, 2401739. <https://doi.org/10.1002/aenm.202401739>.
4. T. Correia and Q. Zhang, eds. (2014). *Electrocaloric Materials: New Generation of Coolers* (Springer).
5. Zhang, T., Li, W., Cao, W., Hou, Y., Yu, Y., and Fei, W. (2016). Giant electrocaloric effect in PZT bilayer thin films by utilizing the electric field engineering. *Appl. Phys. Lett.* 108, 162902. <https://doi.org/10.1063/1.4947446>.
6. Correia, T.M., Kar-Narayan, S., Young, J.S., Scott, J.F., Mathur, N.D., Whatmore, R.W., and Zhang, Q. (2011). PST thin films for electrocaloric coolers. *J. Phys. D Appl. Phys.* 44, 165407. <https://doi.org/10.1088/0022-3727/44/16/165407>.
7. Sadl, M., Prah, U., Kovacova, V., Defay, E., Rojac, T., Lebar, A., Valentincic, J., and Ursic, H. (2023). Multifunctional flexible ferroelectric thick-film structures with energy storage, piezoelectric and electrocaloric performance. *J. Mater. Chem. C* 11, 10058–10068. <https://doi.org/10.1039/D3TC01555F>.
8. Prah, U., Sadl, M., Torello, A., Lheritier, P., Kovacova, V., Ursic, H., and Defay, E. (2023). Direct Electrocaloric Characterization of Ceramic Films. *Small Methods* 7, 2300212. <https://doi.org/10.1002/smt.202300212>.
9. Sadl, M., Lebar, A., Valentincic, J., and Ursic, H. (2022). Flexible Energy-Storage Ceramic Thick-Film Structures with High Flexural Fatigue Endurance. *ACS Appl. Energy Mater.* 5, 6896–6902. <https://doi.org/10.1021/acsaem.2c00518>.

10. Pérez-Martín, Y., Peláiz-Barranco, A., García-Zaldívar, O., Calderón-Piñar, F., Yang, T., Paiva, P.M., Silva, A.C., and Guerra, J.D.S. (2023). Electrocaloric effect, pyroelectric response and energy storage performance of lanthanum-modified PZT relaxor ferroelectric ceramic. *Phys. B Condens. Matter* 671, 415420. <https://doi.org/10.1016/j.physb.2023.415420>.
11. Li, J., Torelló, A., Kovacova, V., Prah, U., Aravindhan, A., Granzow, T., Usui, T., Hirose, S., and Defay, E. (2023). High cooling performance in a double-loop electrocaloric heat pump. *Science* 382, 801–805. <https://doi.org/10.1126/science.adf5477>.
12. Sarkar, A., Šadl, M., Jazbec, A., Snoj, L., Drnovšek, S., Rojac, T., Brennecka, G.L., Uršič, H., and Malič, B. (2023). Influence of neutron and gamma irradiation on the electrocaloric properties of Mn-doped $0.9\text{Pb}(\text{Mg}_{1/3}\text{Nb}_{2/3})\text{O}_3-0.1\text{PbTiO}_3$ ceramics. *JPhys Energy* 5, 045006. <https://doi.org/10.1088/2515-7655/acf61b>.
13. Uršič, H., Vrabelj, M., Otoničar, M., Fulanović, L., Rožič, B., Kutnjak, Z., Bobnar, V., and Malič, B. (2021). Influence of synthesis-related microstructural features on the electrocaloric effect for $0.9\text{Pb}(\text{Mg}_{1/3}\text{Nb}_{2/3})\text{O}_3-0.1\text{PbTiO}_3$ ceramics. *Crystals* 11, 372. <https://doi.org/10.3390/cryst11040372>.
14. Vrabelj, M., Fulanović, L., Bradeško, A., Drnovšek, S., and Malič, B. (2015). Specific Heat Capacity and Thermal Conductivity of the Electrocaloric (1-x)Pb(Mg_{1/3}Nb_{2/3})O₃-xPbTiO₃ Ceramics Between Room Temperature and 300 °C. *Inf. MIDEM* 45, 260–265.
15. Uršič, H., Prah, U., Rojac, T., Jazbec, A., Snoj, L., Drnovšek, S., Bradeško, A., Mirjanič, A., Vrabelj, M., and Malič, B. (2022). High radiation tolerance of electrocaloric (1-x)Pb(Mg_{1/3}Nb_{2/3})O₃-xPbTiO₃. *J. Eur. Ceram. Soc.* 42, 5575–5583. <https://doi.org/10.1016/j.jeurceramsoc.2022.05.051>.
16. Vrabelj, M., Uršič, H., Kutnjak, Z., Rožič, B., Drnovšek, S., Benčan, A., Bobnar, V., Fulanović, L., and Malič, B. (2016). Large electrocaloric effect in grain-size-engineered $0.9\text{Pb}(\text{Mg}_{1/3}\text{Nb}_{2/3})\text{O}_3-0.1\text{PbTiO}_3$. *J. Eur. Ceram. Soc.* 36, 75–80. <https://doi.org/10.1016/j.jeurceramsoc.2015.09.031>.
17. Regis, V., Šadl, M., Brennecka, G., Bradeško, A., Tomc, U., and Uršič, H. (2023). Investigation of Structural and Electrical Properties of Al₂O₃/Al Composites Prepared by Aerosol Co-Deposition. *Crystals* 13, 850. <https://doi.org/10.3390/cryst13050850>.
18. Šadl, M., Condurache, O., Bencan, A., Dragomir, M., Prah, U., Malič, B., Deluca, M., Eckstein, U., Hausmann, D., Khansur, N.H., et al. (2021). Energy-storage-efficient $0.9\text{Pb}(\text{Mg}_{1/3}\text{Nb}_{2/3})\text{O}_3-0.1\text{PbTiO}_3$ thick films integrated directly onto stainless steel. *Acta Mater.* 221, 117403. <https://doi.org/10.1016/j.actamat.2021.117403>.
19. Tan, W.K., Shigeta, Y., Yokoi, A., Kawamura, G., Matsuda, A., and Muto, H. (2019). Investigation of the anchor layer formation on different substrates and its feasibility for optical properties control by aerosol deposition. *Appl. Surf. Sci.* 483, 212–218. <https://doi.org/10.1016/j.apsusc.2019.03.278>.
20. Exner, J., Hahn, M., Schubert, M., Hanft, D., Fuierer, P., and Moos, R. (2015). Powder requirements for aerosol deposition of alumina films. *Adv. Powder Technol.* 26, 1143–1151. <https://doi.org/10.1016/j.apt.2015.05.016>.
21. Exner, J., Linz, M., Kita, J., and Moos, R. (2021). Making powder aerosol deposition accessible for small amounts: A novel and modular approach to produce dense ceramic films. *Int. J. Appl. Ceram. Technol.* 18, 2178–2196. <https://doi.org/10.1111/ijac.13841>.
22. Hatono, H., Ito, T., Iwata, K., and Akedo, J. (2006). Multilayer Construction with Various Ceramic Films for Electronic Devices Fabricated by Aerosol Deposition. *Int. J. Appl. Ceram. Technol.* 3, 419–427. <https://doi.org/10.1111/j.1744-7402.2006.02109.x>.
23. Šadl, M., Tomc, U., Prah, U., and Ursic, H. (2019). Protective alumina coatings prepared by aerosol deposition on magnetocaloric gadolinium elements. *Inf. MIDEM* 49, 177–182. <https://doi.org/10.33180/infmidem2019.306>.
24. Maiorino, A., Del Duca, M.G., Tomc, U., Tušek, J., Kitanovski, A., and Aprea, C. (2021). A numerical modelling of a multi-layer LaFeCoSi Active magnetic regenerator by using Artificial Neural Networks. *Appl. Therm. Eng.* 197, 117375. <https://doi.org/10.1016/j.applthermaleng.2021.117375>.
25. Peixer, G.F., Tomc, U., Kitanovski, A., Lozano, J.A., and Barbosa, J.R. (2025). AI-driven Monte Carlo uncertainty analysis of Curie temperature effects on active magnetic regenerator performance. *Int. J. Refrig.* 180, 518–527. <https://doi.org/10.1016/j.ijrefrig.2025.09.011>.
26. Petelin, N., Pečar, B., Vrtačnik, D., Perne, J., Tomc, U., and Kitanovski, A. (2024). Oscillating thermal switch using electrostatic forces. *J. Phys., Conf. Ser.* 2766, 012204. <https://doi.org/10.1088/1742-6596/2766/1/012204>.
27. Nielsen, K.K., Tusek, J., Engelbrecht, K., Schopfer, S., Kitanovski, A., Bahl, C.R.H., Smith, A., Pryds, N., and Poredos, A. (2011). Review on numerical modeling of active magnetic regenerators for room temperature applications. *Int. J. Refrig.* 34, 603–616. <https://doi.org/10.1016/j.ijrefrig.2010.12.026>.
28. Tomc, U., Peixer, G.F., Bahl, C.R.H., Nielsen, K.K., Lozano, J.A., Barbosa, J.R., and Kitanovski, A. (2025). Influence of Layering and Curie Temperature Uncertainty on the Performance of Multilayer Active Magnetic Regenerators. *Adv. Funct. Mater.* 35, e24282. <https://doi.org/10.1002/adfm.202424282>.
29. Aravindhan, A., Lheritier, P., Torelló, A., Prah, U., Nouchokgwe, Y., El Moul, A., Chevalier, X., Domingues Dos Santos, F., Defay, E., and Kovacova, V. (2023). Direct measurement of electrocaloric effect in P(VDF-TrFE-CFE) film using infrared imaging. *J. Materiomics* 9, 256–260. <https://doi.org/10.1016/j.jmat.2022.10.009>.
30. Vives, E., Burrows, S., Edwards, R.S., Dixon, S., Mañosa, L., Planes, A., and Romero, R. (2011). Temperature contour maps at the strain-induced martensitic transition of a Cu–Zn–Al shape-memory single crystal. *Appl. Phys. Lett.* 98, 011902. <https://doi.org/10.1063/1.3533403>.
31. Mañosa, L., and Planes, A. (2017). Materials with Giant Mechanocaloric Effects: Cooling by Strength. *Adv. Mater.* 29, 1603607. <https://doi.org/10.1002/adma.201603607>.
32. Gràcia-Condal, A., Planes, A., Mañosa, L., Wei, Z., Guo, J., Soto-Parra, D., and Liu, J. (2022). Magnetic and structural entropy contributions to the multicaloric effects in Ni-Mn-Ga-Cu. *Phys. Rev. Mater.* 6, 084403. <https://doi.org/10.1103/PhysRevMaterials.6.084403>.
33. Lünser, K., Kavak, E., Gürpınar, K., Emre, B., Atakol, O., Stern-Taulats, E., Porta, M., Planes, A., Lloveras, P., Tamarit, J.-L., and Mañosa, L. (2024). Elastocaloric, barocaloric and magnetocaloric effects in cross-over polymer composite films. *Nat. Commun.* 15, 6171. <https://doi.org/10.1038/s41467-024-50373-2>.
34. Valdés, E., Stern-Taulats, E., Candau, N., Mañosa, L., and Vives, E. (2024). Enhancement of the Elastocaloric Performance of Natural Rubber by Forced Air Convection. *Polymers* 16, 3078. <https://doi.org/10.3390/polym16213078>.
35. Wei, Z.Y., Sun, W., Shen, Q., Shen, Y., Zhang, Y.F., Liu, E.K., and Liu, J. (2019). Elastocaloric effect of all-d-metal Heusler NiMnTi(Co) magnetic shape memory alloys by digital image correlation and infrared thermography. *Appl. Phys. Lett.* 114, 101903. <https://doi.org/10.1063/1.5077076>.
36. Pereira, M.J., Santos, T., Correia, R., Amaral, J.S., Amaral, V.S., Fabbri, S., and Albertini, F. (2023). Mapping the magnetocaloric effect at the micro-scale on a ferromagnetic shape memory alloy with infrared thermography. *JPhys Mater.* 6, 024002. <https://doi.org/10.1088/2515-7639/acc13b>.
37. Tušek, J., Engelbrecht, K., and Pryds, N. (2016). Elastocaloric effect of a Ni-Ti plate to be applied in a regenerator-based cooling device. *Sci. Technol. Built Environ.* 22, 489–499. <https://doi.org/10.1080/23744731.2016.1176809>.
38. Ianniciello, L., Romanini, M., Mañosa, L., Planes, A., Engelbrecht, K., and Vives, E. (2020). Tracking the dynamics of power sources and sinks during the martensitic transformation of a Cu–Al–Ni single crystal. *Appl. Phys. Lett.* 116, 183901. <https://doi.org/10.1063/5.0006859>.
39. Ossmer, H., Lambrecht, F., Gültig, M., Chluba, C., Quandt, E., and Kohl, M. (2014). Evolution of temperature profiles in TiNi films for elastocaloric

- cooling. *Acta Mater.* *81*, 9–20. <https://doi.org/10.1016/j.actamat.2014.08.006>.
40. Hirai, T., Iguchi, R., Miura, A., and Uchida, K. (2022). Elastocaloric Kirigami Temperature Modulator. *Adv. Funct. Mater.* *32*, 2201116. <https://doi.org/10.1002/adfm.202201116>.
 41. Regis, V., Brennecke, G., Tomc, U., Kitanovski, A., Cerar, J., Tušek, J., Jerman, I., Stern-Taulats, E., Lünser, K., Mañosa, L., and Uršič, H. (2025). Airbrushing: A Novel Method for Preparation of High-Emissivity Black Coating for Infrared Measurements. *Adv. Mater. Interfac.* *12*, e00467. <https://doi.org/10.1002/admi.202500467>.
 42. Blaine, R.L. (2018). In search of thermal effusivity reference materials. *J. Therm. Anal. Calorim.* *132*, 1419–1422. <https://doi.org/10.1007/s10973-018-7020-6>.
 43. Ziambaras, E., and Hyldgaard, P. (2006). Phonon Knudsen flow in nanostructured semiconductor systems. *J. Appl. Phys.* *99*, 054303. <https://doi.org/10.1063/1.2175474>.
 44. Moffett, M.B., Robinson, H.C., Powers, J.M., and Baird, P.D. (2007). Single-crystal lead magnesium niobate-lead titanate (PMN/PT) as a broadband high power transduction material. *J. Acoust. Soc. Am.* *121*, 2591–2599. <https://doi.org/10.1121/1.2717496>.
 45. Poletkin, K.V., Gurzadyan, G.G., Shang, J., and Kulish, V. (2012). Ultrafast heat transfer on nanoscale in thin gold films. *Appl. Phys. B* *107*, 137–143. <https://doi.org/10.1007/s00340-011-4862-z>.
 46. Huber, R.C., Dattelbaum, D.M., Lang, J.M., Coe, J.D., Peterson, J.H., Bartram, B., and Gibson, L.L. (2023). Polyimide dynamically compressed to decomposition pressures: Two-wave structures captured by velocimetry and modeling. *J. Appl. Phys.* *133*, 035106. <https://doi.org/10.1063/5.0128515>.
 47. Cottrill, A.L., Liu, A.T., Kunai, Y., Koman, V.B., Kaplan, A., Mahajan, S.G., Liu, P., Toland, A.R., and Strano, M.S. (2018). Ultra-high thermal effusivity materials for resonant ambient thermal energy harvesting. *Nat. Commun.* *9*, 664. <https://doi.org/10.1038/s41467-018-03029-x>.
 48. Walters, R.N., and Lyon, R.E. (2003). Molar group contributions to polymer flammability. *J. Appl. Polym. Sci.* *87*, 548–563. <https://doi.org/10.1002/app.11466>.
 49. Hsu, K.-L., Kline, D.E., and Tomlinson, J.N. (1965). Thermal conductivity of polytetrafluoroethylene. *J. Appl. Polym. Sci.* *9*, 3567–3574. <https://doi.org/10.1002/app.1965.070091106>.
 50. Fai Lau, S., Suzuki, H., and Wunderlich, B. (1984). The thermodynamic properties of polytetrafluoroethylene. *J. Polym. Sci. Polym. Phys. Ed.* *22*, 379–405. <https://doi.org/10.1002/pol.1984.180220305>.
 51. Wu, M., Liang, Y., Jiang, J.-Z., and Tse, J.S. (2012). Structure and Properties of Dense Silica Glass. *Sci. Rep.* *2*, 398. <https://doi.org/10.1038/srep00398>.
 52. Andersson, S., and Dzhavadov, L. (1992). Thermal conductivity and heat capacity of amorphous SiO₂ : pressure and volume dependence. *J. Phys. Condens. Matter* *4*, 6209–6216. <https://doi.org/10.1088/0953-8984/4/29/005>.
 53. Dan'kov, S.Y., Tishin, A.M., Pecharsky, V.K., and Gschneidner, K.A. (1998). Magnetic phase transitions and the magnetothermal properties of gadolinium. *Phys. Rev. B* *57*, 3478–3490. <https://doi.org/10.1103/PhysRevB.57.3478>.
 54. Jacobsson, P., and Sundqvist, B. (1989). Thermal conductivity and electrical resistivity of gadolinium as functions of pressure and temperature. *Phys. Rev. B* *40*, 9541–9551. <https://doi.org/10.1103/PhysRevB.40.9541>.
 55. Hu, Y., Du, G., and Chen, N. (2016). A novel approach for Al₂O₃/epoxy composites with high strength and thermal conductivity. *Compos. Sci. Technol.* *124*, 36–43. <https://doi.org/10.1016/j.compscitech.2016.01.010>.
 56. Galusek, D., and Galusková, D. (2015). Alumina Matrix Composites with Non-Oxide Nanoparticle Addition and Enhanced Functionalities. *Nanomaterials* *5*, 115–143. <https://doi.org/10.3390/nano5010115>.
 57. Yao, Y., Zeng, X., Guo, K., Sun, R., and Xu, J.b. (2015). The effect of interfacial state on the thermal conductivity of functionalized Al₂O₃ filled glass fibers reinforced polymer composites. *Composites Part A* *69*, 49–55. <https://doi.org/10.1016/j.compositesa.2014.10.027>.
 58. Gustavsson, M., Karawacki, E., and Gustafsson, S.E. (1994). Thermal conductivity, thermal diffusivity, and specific heat of thin samples from transient measurements with hot disk sensors. *Rev. Sci. Instrum.* *65*, 3856–3859. <https://doi.org/10.1063/1.1145178>.
 59. Chang, Y.A., and Hultgren, R. (1965). The Dilation Contribution to the Heat Capacity of Copper and α -Brass at Elevated Temperatures¹. *J. Phys. Chem.* *69*, 4162–4165. <https://doi.org/10.1021/j100782a017>.
 60. Mathot, V.B.F., and Pijpers, M.F.J. (1983). Heat capacity, enthalpy and crystallinity for a linear polyethylene obtained by DSC. *J. Therm. Anal.* *28*, 349–358. <https://doi.org/10.1007/BF01983270>.
 61. Regis, V., and Uršič, H. (2026). Roadmap for Electrocaloric Films Characterization: A Numerical Study (Zenodo). <https://doi.org/10.5281/ZENODO.18233561>.

STAR★METHODS

KEY RESOURCES TABLE

REAGENT or RESOURCE	SOURCE	IDENTIFIER
Deposited data		
Raw data	This paper	https://doi.org/10.5281/zenodo.18245578
Software and algorithms		
COMSOL Multiphysics	COMSOL AB	comsol.com
Python 3	Python Software Foundation	python.org
Other		
SEM Verios HP 4G	Thermo Fisher Scientific	thermofisher.com
Acrylic black paint	Vallejo	70.602
DSC 204 F1	Netsch Group	netsch.com

METHOD DETAILS

Scanning electron microscopy

The cross-section of the reference sample was analyzed using a scanning electron microscope (SEM; Verios HP 4G, ThermoFisher, USA). Prior to the imaging, the sample was prepared into an epoxy resin matrix and fine polished.

Numerical modelling

The heat flow dynamics of the caloric system was simulated via a 2-dimensional finite-element model (COMSOL® Multiphysics version 6.2) using the thermal management module and time-dependent solver, within the interval 0 s to 50 ms at 10 μ s steps. In all cases, the substrate had a fixed thickness of 125 μ m, and a 1 μ m-thick gold bottom electrode, the width of all layers was set to 5 mm. It is worth emphasizing that in the case of aerosol-deposited films, considered the reference structure, the thickness of the top electrode is at most \sim 0.1 μ m and, therefore, it was not implemented in the simulations. The influence of contacts for voltage application was assumed to be negligible, and all surrounding edges of the system were considered thermally insulated.

QUANTIFICATION AND STATISTICAL ANALYSIS

The simulation data is produced by COMSOL Multiphysics. Figures shown in the main text were produced in Python and Microsoft PowerPoint.